# Nanoscale

## PAPER

Check for updates

# A 3D mixed ion-electron conducting framework for dendrite-free lithium metal anodes†

Jinmin Lin,[a] Zerui Chen,[a] Wei Zhao,[a] Junwei Han,[a] Bo Chen,[c] Yao Chen,[c] Qianqian Liu*[b] and Hao Bin Wu ✪ *[a,d]

To enable the practical application of lithium metal batteries, it is crucial to address the challenges of dendrite growth and volume expansion in lithium metal anodes. A 3D framework offers an effective solution to regulate the lithium plating/stripping process. In this work, we present a 3D mixed ion-electron conducting (MIEC) framework as a lithium metal anode, achieved by conformally coating carbon nanotubes (CNTs) onto $Li_{0.5}La_{0.5}TiO_3$ (LLTO) particles. The synergy between LLTO's lithiophilicity and CNTs' high electron conductivity ensures uniform lithium deposition and mitigates volume changes, thereby enhancing the electrochemical performance. As a result, the LLTO@CNT anode demonstrates a high coulombic efficiency of 99.24% for 400 cycles at 1 mA cm$^{-2}$ in a half-cell, along with excellent cycling stability and prolonged lifespan.

[a]*Institute for Composites Science Innovation (InCSI) and State Key Laboratory of Silicon Materials, School of Materials Science and Engineering, Zhejiang University, Hangzhou, China. E-mail: hbwu@zju.edu.cn*
[b]*Key Laboratory of Electronic Materials and Devices of Tianjin, School of Electronics and Information Engineering, Hebei University of Technology, Tianjin, China*
[c]*Zhejiang Cosmx Battery Co., Ltd, Jiaxing, China*
[d]*Zhejiang Key Laboratory of Advanced Solid State Energy Storage Technology and Applications, Taizhou Institute of Zhejiang University, Taizhou 318000, China*
†Electronic supplementary information (ESI) available: Experimental methods, SEM data, EDS data, EIS profiles and CV profiles. See DOI: https://doi.org/10.1039/d4nr04455j

*Dr. Hao Bin Wu is a tenured associate professor in the School of Materials Science and Engineering at Zhejiang University. He received his B.S. degree from Fudan University in 2010, and Ph.D. from Nanyang Technological University in 2015. He conducted postdoctoral research at the University of California, Los Angeles, before joining Zhejiang University in 2017.*

**Hao Bin Wu**

*Dr. Wu's research focuses on advanced electrochemical energy storage and conversion technologies, with particular emphasis on lithium batteries and $CO_2$ electrolysis. He has co-authored over 160 publications with an H-index of 89. He was recognized as a Clarivate Analytics' Highly Cited Researcher from 2017 to 2024.*

## Introduction

The growing demand for high-end electronic devices and electric vehicles has driven intensive research into high-energy-density batteries, with significant attention given to lithium metal anodes (LMAs) due to their highest theoretical specific capacity (3860 mA h g$^{-1}$) and lowest potential (−3.04 V *vs.* standard hydrogen electrode).[1,2] However, several critical challenges hinder their practical applications, including the growth of lithium dendrites, side reactions at the unstable Li–electrolyte interface, and severe volume change during cycling.[3,4] These issues not only lead to the degradation of battery performance in terms of shortened lifespan and reduced capacity but also pose significant safety risks, such as short circuits and explosions.[5,6]

Over the years, various strategies have been developed to address these challenges of LMAs, particularly focusing on composition modifications of liquid electrolytes, adaptation of solid-state electrolytes, modulation of artificial solid-electrolyte interphase (SEI), separator engineering, and construction of 3D porous frameworks.[7–10] Among these, 3D frameworks have emerged as a promising solution, which simultaneously facilitate uniform lithium plating and accommodate electrode volume change, thus enhancing structural stability.[11,12]

Generally, 3D frameworks can be categorized into three types: conductive hosts, lithiophilic hosts and mixed ion-electron conductive (MIEC) hosts. Conductive hosts are the most commonly used, which delay dendrite formation through reducing local current density by the high specific surface area. Additionally, they ensure a uniform electric field distribution, promoting the even deposition of Li.[13,14] However, in

conventional conductive hosts, the kinetics of ion transport are slower than that of electron transport, leading to surface Li deposition and continuous upward growth, which increases the risk of short circuits.[15] To enhance Li$^+$ absorption, lithiophilic hosts have been developed.[16,17] These frameworks are characterized by abundant Li$^+$ channels and polar functional groups, offering both high lithiophilicity and excellent ionic conductivity to modulate the distribution of Li$^+$.[18–20] However, their poor electronic conductivity might result in lithium deposition at the bottom of the framework, potentially causing uneven Li deposition and detachment of porous frameworks from the current collector (Fig. 1a).[12] MIEC hosts, which combine lithiophilicity and electron conductivity, offer synergistic benefits of both properties.[21–23] For example, Ouyang[24] reported a C@ZnOnts@CC MIEC anode, delivering stable cycling with an average coulombic efficiency (CE) of 98.54% for 150 cycles at 4 mA h cm$^{-2}$ in a half-cell. Cheng[22] reported a Cu$_2$S@CC MIEC scaffold, which exhibited a high CE of 99.27% for 450 cycles at 1 mA h cm$^{-2}$. Nevertheless, the development of appropriate frameworks with high lithiophilicity, high capacity, and long cycling stability remains a challenge.

In this work, we developed a 3D porous MIEC scaffold composed of Li$_{0.5}$La$_{0.5}$TiO$_3$ (LLTO) particles with a conformal CNT coating, prepared by a simple casting method (Fig. 1b). LLTO with high ionic conductivity offers abundant Li$^+$ migration pathways and undergoes a transition from an insulator to a conductor upon Li$^+$ insertion. This transformation enhances the lithiophilicity of LLTO and reduces nucleation overpotential during lithium deposition. The CNT layer further improves electron conductivity, enabling efficient charge transport. The combined effect of LLTO and CNTs ensures balanced electron and ion distribution, thereby mitigating the issues associated with conventional LMAs during cycling. The LLTO@CNT MIEC framework demonstrated exceptional electrochemical performance, including a low overpotential and a high coulombic efficiency of 99.24% for 400 cycles. This mixed-conductive anode design significantly enhanced both cycling stability and rate performance, addressing the key limitations of LMAs.

# Results and discussion

The LLTO powder was prepared by a simple ball-milling and sintering process. Fig. 2a shows the morphology of pristine LLTO particles, which exhibit irregular, flat shapes with smooth surfaces and sizes of 5–8 μm. Elemental mappings confirm the uniform distribution of La, Ti and O throughout the LLTO particles (Fig. S1†). X-ray diffraction (XRD) analysis (Fig. 2b) confirmed the crystalline structure of LLTO consisting of two phases. The major peaks are attributed to the tetragonal perovskite Li$_{0.5}$La$_{0.5}$TiO$_3$, a phase known for its high ionic conductivity. The minor peaks can be assigned to layered perovskite Li$_2$La$_2$Ti$_3$O$_{10}$, which formed due to the use of excess Li$_2$CO$_3$ during synthesis.[25] The layered perovskite phase has been reported to enhance grain boundary conduction, further contributing to the overall ionic conductivity. Electrochemical impedance spectroscopy (EIS) was used to evaluate the ionic conductivity. As shown in Fig. 2c, the as-prepared LLTO exhibits higher ionic conductivity compared to a commercially available LLTO sample, demonstrating the effectiveness of our synthesis process.

To construct a porous electrode, polymethyl methacrylate (PMMA) spheres were added as a porogen. Without the addition of CNTs, the LLTO particles retained their smooth surfaces (Fig. 2d and Fig. S2a†). After introducing CNTs (Fig. 2e and f), the surface becomes rough with CNTs forming a conformal coating over the particles (Fig. S2b†). The interconnected LLTO particles and CNTs form continuous pathways for both electron and Li-ion transport, thereby forming a MIEC framework. Scanning electron microscopy (SEM) revealed numerous pores with diameters in the range of 5–10 μm, which provide sufficient space to accommodate lithium metal. The porosity of the electrode was found to be about 46% using an absorption method.

To investigate lithium deposition behavior on different substrates, half-cells were assembled with three different anodes, namely LLTO, LLTO@CNT and Cu foil. A localized high concentration electrolyte (PFPN-DHCE) was used to minimize the side reactions during lithium deposition.[26] Fig. 3 depicts the
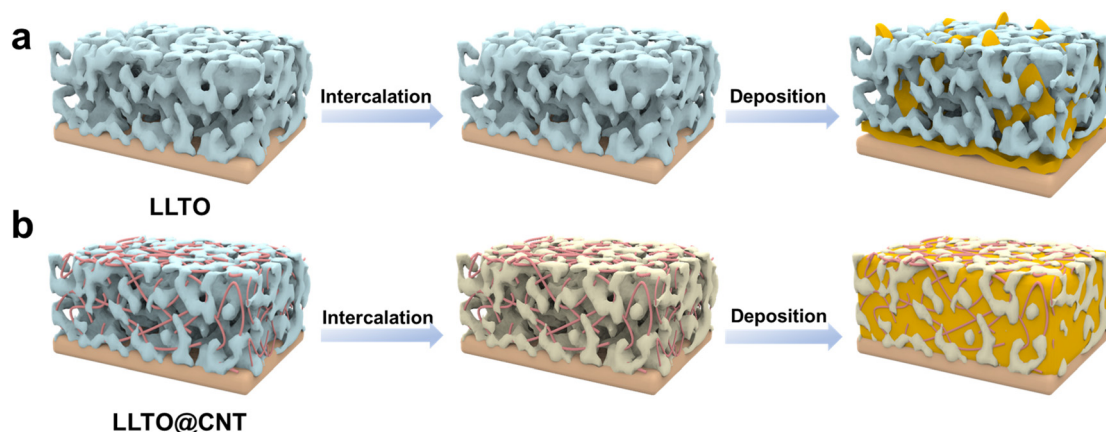


**Fig. 1** Schematic illustration of Li deposition on (a) LLTO and (b) LLTO@CNT MIEC frameworks.
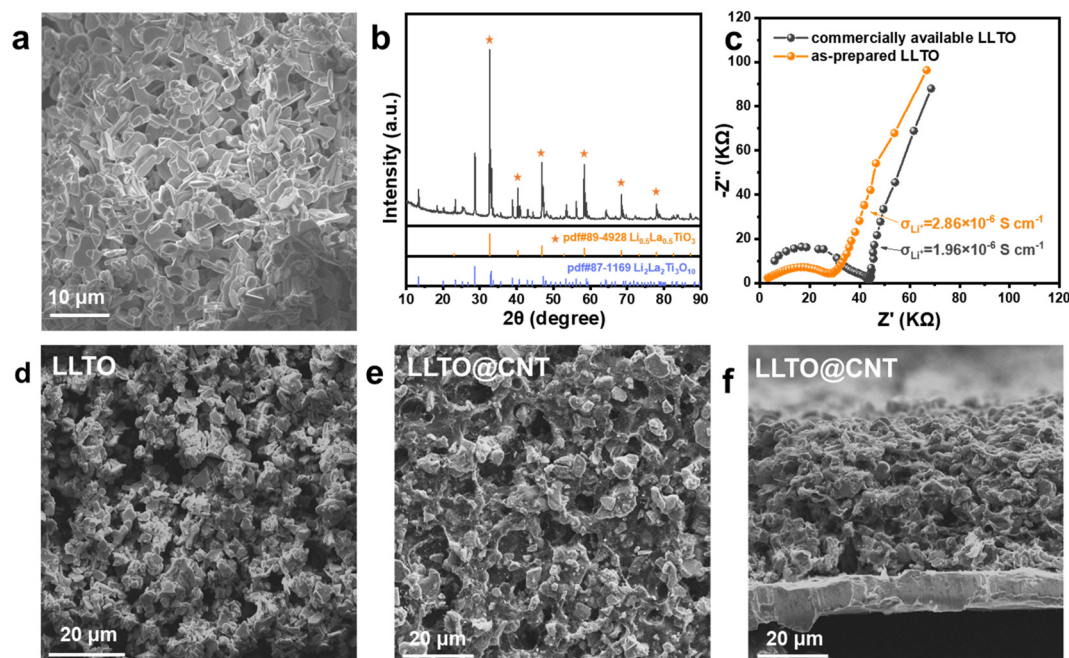
**Fig. 2** (a) SEM image and (b) XRD pattern of the as-prepared LLTO particles. (c) Nyquist plot of the as-prepared LLTO and commercially available LLTO. (d) Surface SEM image of the LLTO electrode without CNTs. (e) Surface and (f) cross-sectional SEM images of the LLTO@CNT MIEC electrode.
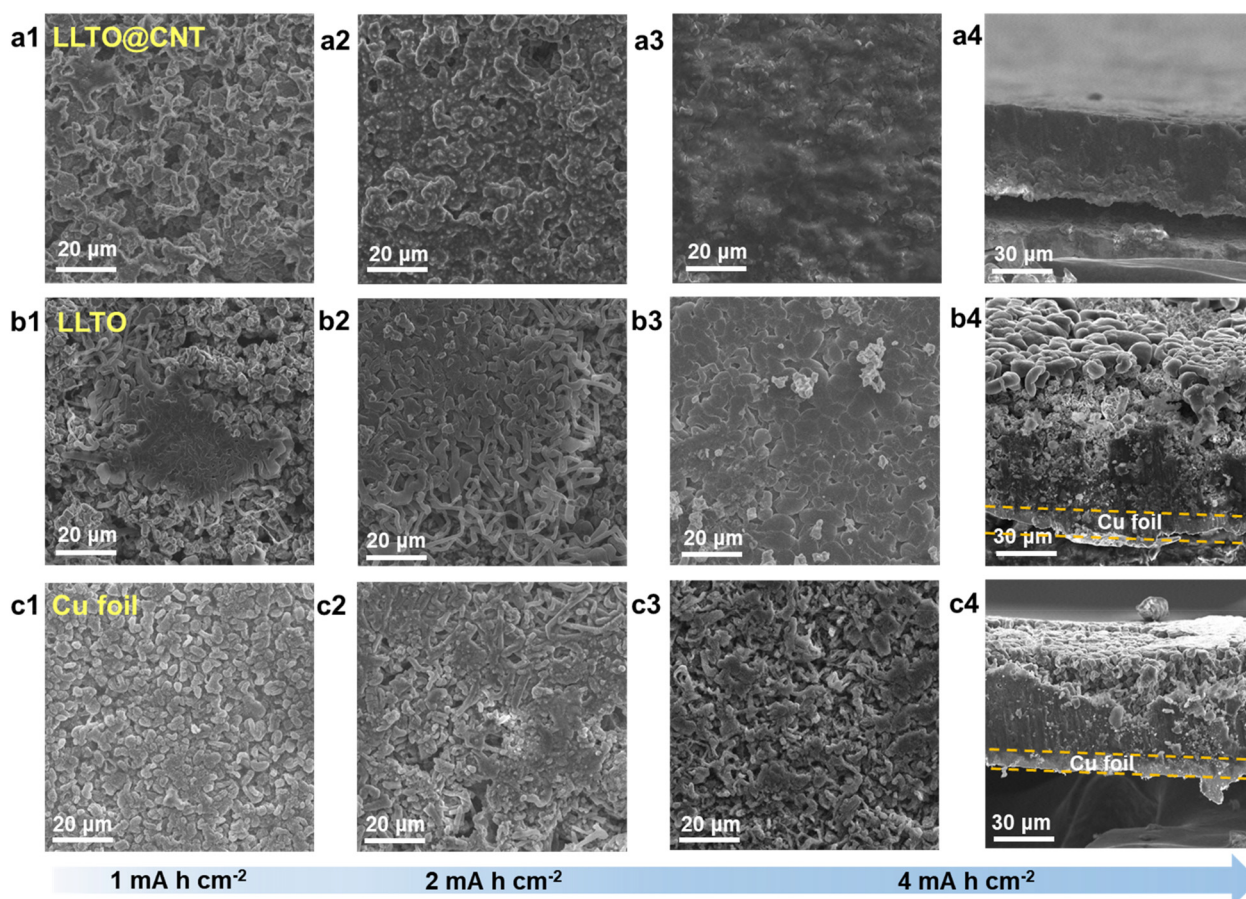


**Fig. 3** Surface morphologies of (a1–a3) LLTO@CNT, (b1–b3) LLTO and (c1–c3) Cu foil after depositing (a1, b1 and c1) 1 mA h cm$^{-2}$, (a2, b2 and c2) 2 mA h cm$^{-2}$, and (a3, b3 and c3) 4 mA h cm$^{-2}$ of Li. Cross-sectional morphologies of (a4) LLTO@CNT, (b4) LLTO and (c4) Cu foil after depositing 4 mA h cm$^{-2}$ of Li.

electrode morphology after plating various capacities of Li at a current density of 0.5 mA cm$^{-2}$. For the LLTO@CNT framework (Fig. 3a1–a3), plating 1 mA h cm$^{-2}$ of Li leads to the encapsulation of LLTO particles and enlarged particle size. As the capacity increases to 2 mA h cm$^{-2}$, lithium begins to fill the pores in the framework, making the electrode more compact. At 4 mA h cm$^{-2}$, lithium nearly saturates the entire framework, exhibiting a smooth surface texture without lithium dendrites. A cross-sectional view clearly reveals that the Li metal uniformly and densely fills the interior of the framework while maintaining a flat surface (Fig. 3a4). Such a deposition pattern arises from the synergistic effect of the lithiophilicity of LLTO and the conductivity of CNTs, which together form mixed conductive pathways. The MIEC framework not only provides abundant nucleation sites but also enhances the Li$^+$ transport kinetics, resulting in optimized lithium deposition behavior.

In contrast, the pure LLTO framework without CNT coating shows a markedly different deposition pattern (Fig. 3b). Due to the poor electronic conductivity of LLTO, Li initially deposits at the bottom on the Cu foil, which may cause detachment of the LLTO framework from the Cu foil. The deposition is irregular, and lithium starts to deposit on the upper surface once an electronic pathway forms, leaving a porous interior structure. The clear shape of the LLTO particles without notable Li deposition indicates the absence of sufficient nucleation sites, as the LLTO alone cannot fully lithiate and thus fails to achieve high lithiophilicity. As for the Li deposition on pure Cu foil (Fig. 3c), lithium grows in a non-uniform, moss-like morphology. This loose and uneven plating promotes dendrite formation, increasing the risk of short circuits and compromising battery safety. Overall, the MIEC framework constructed using LLTO and CNTs maximizes the individual contributions of both components and synergistically facilitates uniform lithium deposition. The combination of LLTO's lithiophilicity and CNTs' high conductivity promotes stable, dense, and dendrite-free Li deposition, significantly improving the safety and performance of LMAs.

Lithium plating/stripping performance was evaluated using coin cells. The initial deposition behavior of lithium metal on different substrates was characterized to elucidate the influence of LLTO on Li nucleation. As shown in Fig. 4a, the LLTO@CNT MIEC substrate exhibits a sloping discharge profile without notable nucleation overpotential, compared to the large nucleation overpotential of 100 mV for the Cu foil. This substantial difference arises from the enhanced lithiophilicity of LLTO particles, facilitated by the redox reaction with lithium, which effectively lowers the nucleation barrier. For comparison, pure LLTO and CNT anodes were also fabricated. The CNT anode shows a relatively high overpotential of 95 mV, attributed to the inherently poor lithiophilicity of carbon materials, in line with previous reports. In the case of the pure LLTO framework, the absence of a conductive agent hinders the lithiation of LLTO particles, resulting in a moderate overpotential of 61 mV. The lithiation behaviors of different anodes were further confirmed by a cyclic voltammetry (CV)

test (Fig. 4b). In the LLTO@CNT anode, two pairs of peaks at 1.16/1.22 V and 1.55/1.6 V are clearly observed, corresponding to the electrochemical insertion/de-insertion of Li$^+$ into different vacancies of LLTO, whereas in the pure LLTO anode these peaks are barely seen (Fig. S3†), indicating the necessity of CNTs to promote the lithiation of LLTO particles. The integrated area of the reduction peak in the initial discharge process is larger than that in the subsequent cycles due to the irreversible electrolyte decomposition, consistent with the low initial CE. The AC impedance spectra in Fig. S4a and b† further reveal the impact of lithium insertion on the conductivity of anodes. The pristine LLTO@CNT anode exhibits a large charge transfer resistance of ~250 Ω. However, the resistance decreases to 100 Ω after discharge, owing to the reduction of Ti$^{4+}$ to Ti$^{3+}$. Such transformation not only improves the lithiophilicity but also enhances the electronic conductivity. In contrast, the pure LLTO anode shows a higher initial charge transfer resistance, which remains relatively high even after lithiation. We also measured the apparent ionic and electronic conductivity of the LLTO@CNT and LLTO anodes using a two-electrode configuration (Fig. S4c–f†). Fig. S4e and f† display the conductivity changes before and after lithiation. The LLTO@CNT anode shows a significant improvement in both ionic and electronic conductivities, increasing by an order of magnitude. Conversely, the pure LLTO anode only exhibits a slight increase in conductivity, consistent with earlier findings.

The change of discharge capacity during cycling was also investigated. The LLTO@CNT anode exhibits a high irreversible capacity in the first cycle and undergoes an activation process, during which the capacity gradually increases with continued cycling (Fig. 4c). The irreversible capacity might be attributed to the formation of SEI on the porous structure as well as irreversible Li insertion into LLTO, which could be mitigated by various prelithiation approaches. Increasing the cut-off voltage facilitates the activation process, reducing the activation time and enabling a more rapid increase in CE. Thus, for the lithium deposition test, the cells were first precycled between 0 and 2.5 V for activation. Fig. 4d presents the charge/discharge profiles at different cycles, except for the first few cycles where the intercalation capacity is lower due to the incompletely activated state. After the initial activation process, the curves overlap well in subsequent cycles, demonstrating excellent stability of the electrode.

The uniform and dendrite-free deposition behavior of the LLTO@CNT anode enables a high CE, a critical parameter for evaluating electrochemical reversibility. Fig. 4e shows the CE performance of various half cells tested at a current density of 1 mA cm$^{-2}$ with an areal capacity of 1 mA h cm$^{-2}$. The LLTO@CNT MIEC anode exhibits improved CE, higher cycling stability and prolonged lifespan compared to other anodes. The CE gradually increases to 99% within the first 15 cycles and then stabilizes at ~99.24% over 400 cycles. In contrast, the Cu foil shows erratic CE behavior: an initial decline followed by an increase above 100%, and then a gradual decrease. The fluctuation of CE indicates an irreversible and unstable
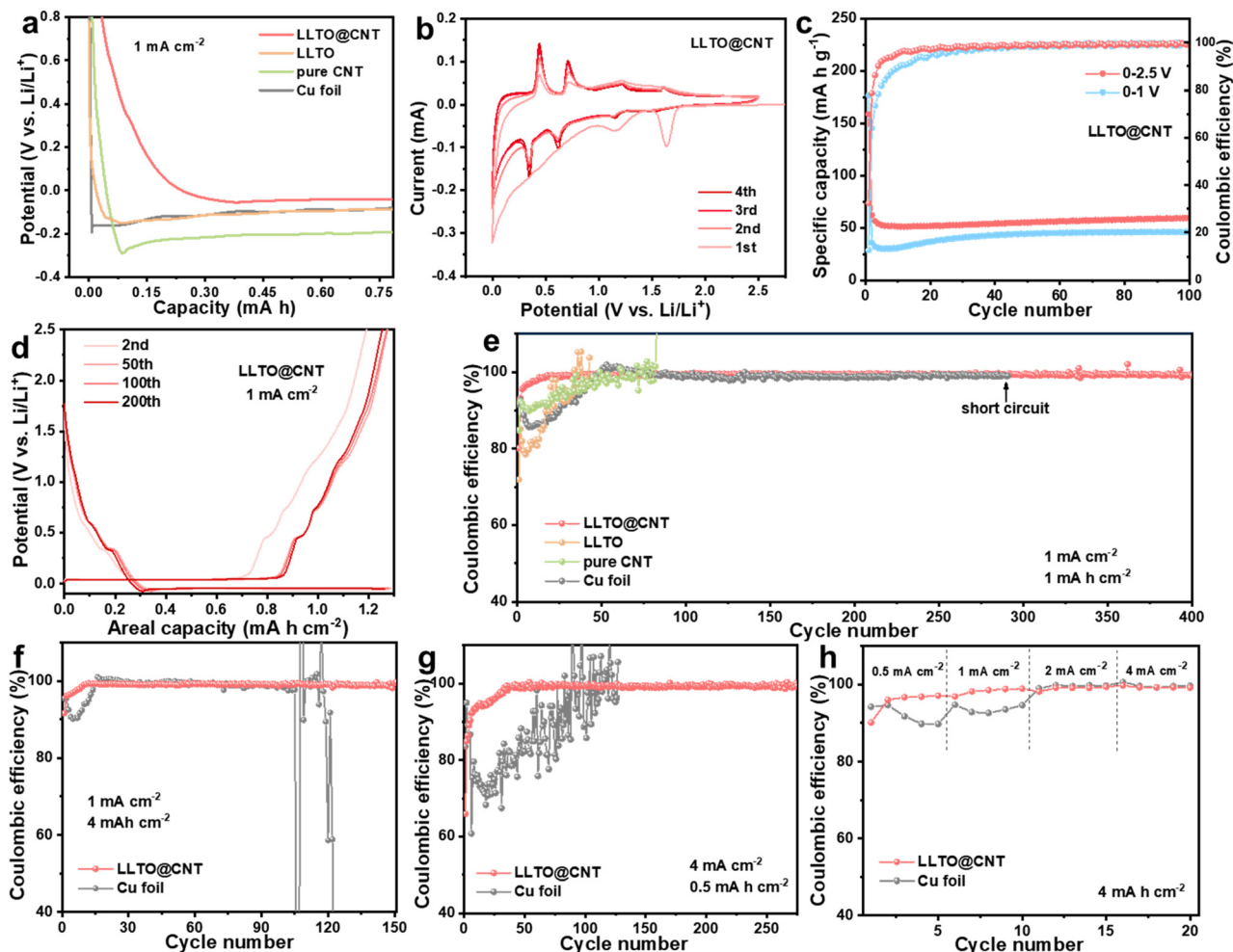
**Fig. 4** (a) Initial discharge profiles on different frameworks. (b) CV curves of the LLTO@CNT anode. (c) Cycling performance of LLTO@CNT at different cut-off voltages. (d) Galvanostatic plating/stripping voltage profiles of Li on the LLTO@CNT anode. (e−g) Coulombic efficiency of Li metal plating/stripping on different anodes cycled at various current densities and areal capacities. (h) Coulombic efficiency of Li metal plating/stripping on the LLTO@CNT anode cycled at 4 mA h cm$^{-2}$ with increasing current densities.

lithium plating/stripping process, which is associated with uncontrolled lithium deposition and dendrite formation. Fig. S5† shows that lithium initially deposits on Cu foil in a disordered, needle-like morphology, contributing to the poor CE during early cycles. Although the localized high-concentration electrolyte used here helps maintain a relatively high CE in later cycles, achieving long-term cycling stability remains a challenge. SEM images of the electrodes after cycling (Fig. S6†) further highlight the advantages of the LLTO@CNT anode. After ten cycles, the 3D porous architecture of the LLTO@CNT anode remains intact, while the Cu foil is covered with a layer of inactive lithium metal, explaining the different cycling performance. Pure LLTO and CNT anodes demonstrate inferior cycling performance with fluctuating CE and limited lifespan (Fig. 4e).

At an increased areal capacity of 4 mA h cm$^{-2}$, the LLTO@CNT MIEC anode maintains a high CE of ~98.97% for 150 cycles, outperforming the Cu foil (Fig. 4f). Similar results

were observed when testing at 2 mA cm$^{-2}$ with an areal capacity of 2 mA h cm$^{-2}$ (Fig. S7†), reinforcing the advantages of the LLTO@CNT anode. Notably, as the current density increases to 4 mA cm$^{-2}$ (Fig. 4g), the MIEC anode achieves a high CE of ~98.59% for 275 cycles, whereas the Cu foil shows apparent instability. The large specific surface area of the 3D framework reduces the local current density and induces uniform deposition, thus enhancing the rate capability of the MIEC anode as verified by the tests at various current densities (Fig. 4h). However, the activation process of LLTO particles is prolonged at high rates, requiring more cycles to reach stable CE, but the CE remains high in subsequent cycles.

To validate the practical application of the LLTO@CNT MIEC anode, full cells were assembled with NCM622 cathodes. Fig. 5a displays the long-term cycling performance of full cells with different anodes at 0.2 C charge/0.5 C discharge between 3.0 and 4.3 V. The LLTO@CNT and Cu foil anodes were pre-plated with lithium to achieve N/P ratios of 4 and 2. At an N/P
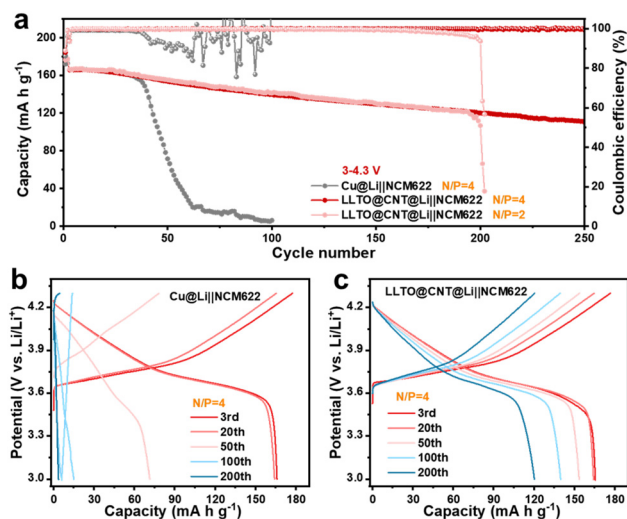
**Fig. 5** (a) The cycling performances of NCM–Li full cells paired with different anodes and cycled between 3.0 and 4.3 V at 0.2 C charge/0.5 C discharge. The corresponding voltage profiles of full cells using (b) the Cu@Li anode and (c) the LLTO@CNT@Li anode.

ratio of 4, the full cell with the Cu@Li anode exhibits rapid capacity decay and an erratic CE after about 35 cycles, which is caused by the poor lithium deposition behavior on the Cu foil. In contrast, the full cell with the LLTO@CNT@Li anode maintains a high capacity retention and stable CE for over 250 cycles. This can be confirmed by the corresponding charge–discharge voltage profiles in Fig. 5b and c. The discharge profiles of the full cell with the Cu@Li anode initially overlap well but rapidly decline in the 50th cycle. In contrast, the full cell with the LLTO@CNT @Li anode shows a gradual and slow decline in the discharge capacity and voltage plateaus over 200 cycles. When the N/P ratio is decreased to 2, the full cell with the MIEC anode still demonstrates remarkable stability, but a sudden capacity drop is observed after 190 cycles. Furthermore, the MIEC anode was tested in an anode-free full cell system, with the LLTO@CNT anode paired with the NCM622 cathode without the pre-deposition of lithium. As shown in Fig. S8,† the anode-free cell exhibits promising performance, achieving a capacity retention of 42% after 100 cycles. While the capacity is lower than that of the pre-lithiated cells, this result represents a meaningful step toward the practical application of LLTO@CNT anodes in anode-free systems.

## Conclusions

In conclusion, we propose a 3D mixed ion-electron conducting (MIEC) framework for lithium metal batteries, effectively addressing the challenges of dendrite growth and volume expansion. The LLTO component provides ion transport channels for lithium migration and enhances the framework's lithiophilicity, while CNTs ensure high electron conductivity. This synergistic combination promotes uniform lithium deposition, enabling the battery to deliver superior performance

under high current densities and large areal capacities. As a result, the MIEC anode exhibits outstanding electrochemical performance, achieving a high coulombic efficiency of 99.24% over 400 cycles at 1 mA $cm^{-2}$ in a half-cell. Furthermore, the full cell demonstrates significantly enhanced cycling stability, maintaining excellent capacity retention for more than 150 cycles. This study offers valuable insights into lithium metal anode design, paving the way for the practical application of lithium metal batteries.

## Author contributions

Jinmin Lin: data curation, investigation, and writing – original draft. Zerui Chen: formal analysis. Wei Zhao: formal analysis. Junwei Han: investigation. Bo Chen: resources. Yao Chen: resources. Qianqian Liu: supervision, funding acquisition, and writing – review and editing. Hao Bin Wu: supervision, funding acquisition, conceptualization, and writing – review and editing.

## Data availability

The data that support the findings of this study are available on request from the corresponding author, H. B. Wu, upon reasonable request.

## Conflicts of interest

There are no conflicts to declare.

## Acknowledgements

## References

1  J. M. Tarascon and M. Armand, *Nature*, 2001, **414**, 359–367.
2  B. Liu and J. Zhang, *Joule*, 2018, **2**, 833–845.
3  J. L. Lang, L. H. Qi, Y. Z. Luo and H. Wu, *Energy Storage Mater.*, 2017, **7**, 115–129.
4  S. J. Yang, X. Min, H. Fan, J. Xiao, Y. A. Liu, R. Y. Mi, X. W. Wu, Z. H. Huang, K. Xi and M. H. Fang, *J. Mater. Chem. A*, 2022, **10**, 17917–17947.

5 W. Xu, J. L. Wang, F. Ding, X. L. Chen, E. Nasybutin, Y. H. Zhang and J. G. Zhang, *Energy Environ. Sci.*, 2014, **7**, 513–537.

6 K. Zhang, F. Wu, K. Zhang, S. T. Weng, X. R. Wang, M. D. Gao, Y. H. Sun, D. Cao, Y. Bai, H. J. Xu, X. F. Wang and C. Wu, *Energy Storage Mater.*, 2021, **41**, 485–494.

7 X. Ji, S. Y. Hou, P. F. Wang, X. Z. He, N. Piao, J. Chen, X. L. Fan and C. S. Wang, *Adv. Mater.*, 2020, **32**, 2002741.

8 C. Chen, Q. W. Liang, G. Wang, D. D. Liu and X. H. Xiong, *Adv. Funct. Mater.*, 2022, **32**, 2107249.

9 D. C. Lin, Y. Y. Liu and Y. Cui, *Nat. Nanotechnol.*, 2017, **12**, 194–206.

10 X. P. Zhang, X. N. Fu, W. F. Tian, Y. Z. Bai, L. Y. Zhu and J. W. Si, *Nanoscale*, 2023, **15**, 15328–15333.

11 Y. F. Cheng, J. B. A. Chen, Y. M. Chen, X. Ke, J. Li, Y. Yang and Z. C. Shi, *Energy Storage Mater.*, 2021, **38**, 276–298.

12 S. Y. Ni, S. S. Tan, Q. Y. An and L. Q. Mai, *J. Energy Chem.*, 2020, **44**, 73–89.

13 W. H. Zhu, W. Deng, F. Zhao, S. S. Liang, X. F. Zhou and Z. P. Liu, *Energy Storage Mater.*, 2019, **21**, 107–114.

14 R. Zhang, X. B. Cheng, C. Z. Zhao, H. J. Peng, J. L. Shi, J. Q. Huang, J. F. Wang, F. Wei and Q. Zhang, *Adv. Mater.*, 2016, **28**, 2155–2162.

15 W. Q. Guo, S. Liu, X. Z. Guan, X. Y. Zhang, X. J. Liu and J. Y. Luo, *Adv. Energy Mater.*, 2019, **9**, 1900193.

16 Y. Wang, J. Tan, Z. H. Li, L. L. Ma, Z. Liu, M. X. Ye and J. F. Shen, *Energy Storage Mater.*, 2022, **53**, 156–182.

17 S. X. Xia, C. W. Yang, Z. Y. Jiang, W. X. Fan, T. Yuan, Y. P. Pang, H. Sun, T. Q. Chen, X. Li and S. Y. Zheng, *Adv. Compos. Hybrid Mater.*, 2023, **6**, 198.

18 Y. Y. Liu, D. C. Lin, Z. Liang, J. Zhao, K. Yan and Y. Cui, *Nat. Commun.*, 2016, **7**, 10992.

19 Y. Zhang, C. W. Wang, G. Pastel, Y. D. Kuang, H. Xie, Y. J. Li, B. Y. Liu, W. Luo, C. J. Chen and L. B. Hu, *Adv. Energy Mater.*, 2018, **8**, 1800635.

20 H. Liu, X. Chen, X. B. Cheng, B. Q. Li, R. Zhang, B. Wang, X. Chen and Q. Zhang, *Small Methods*, 2019, **3**, 7.

21 J. Pu, J. C. Li, K. Zhang, T. Zhang, C. W. Li, H. X. Ma, J. Zhu, P. V. Braun, J. Lu and H. G. Zhang, *Nat. Commun.*, 2019, **10**, 1896.

22 Y. L. Cheng, R. C. Lu, K. Amin, B. B. Zhang, Q. Y. Zhou, C. A. F. Li, L. J. Mao, Z. Zhang, X. Q. Lu and Z. X. Wei, *ACS Appl. Energy Mater.*, 2021, **4**, 6106–6115.

23 C. Y. Zhang, S. Liu, G. J. Li, C. J. Zhang, X. J. Liu and J. Y. Luo, *Adv. Mater.*, 2018, **30**, 1801328.

24 Y. F. Ouyang, S. F. Huang, N. R. Li, S. R. Lu, Y. Lv, Y. R. Liu, F. Y. Kang and Y. D. Cao, *Carbon*, 2024, **229**, 119452.

25 H. Kawai and J. Kuwano, *J. Electrochem. Soc.*, 1994, **141**, L78–LL9.

26 Q. Q. Liu, Y. Liu, Z. R. Chen, Q. Ma, Y. R. Hong, J. H. Wang, Y. F. Xu, W. Zhao, Z. K. Hu, X. Hong, J. W. Wang, X. L. Fan and H. B. Wu, *Adv. Funct. Mater.*, 2023, **33**, 2209725.